Swept-wing transition control using DBD plasma actuators

Yadala, Srikar; Hehner, Marc T.; Serpieri, Jacopo; Benard, Nicolas; Kotsonis, Marios

DOI
10.2514/6.2018-3215

Publication date
2018

Document Version
Accepted author manuscript

Published in
2018 Flow Control Conference

Citation (APA)
Yadala, S., Hehner, M. T., Serpieri, J., Benard, N., & Kotsonis, M. (2018). Swept-wing transition control using DBD plasma actuators. In *2018 Flow Control Conference* Article AIAA 2018-3215 American Institute of Aeronautics and Astronautics Inc. (AIAA). https://doi.org/10.2514/6.2018-3215

Swept-wing transition control using DBD plasma actuators

Srikar Yadala*[1,2], Marc T. Hehner†[1,3], Jacopo Serpieri‡[1], Nicolas Benard§[2], and Marios Kotsonis¶[1]

[1]*AWEP Department, Section of Aerodynamics, Delft University of Technology, Kluyverweg 1, 2629HS Delft, The Netherlands*
[2]*Institut PPRIME, Université de Poitiers (CNRS UPR 3346, ISAE-ENSMA), Boulevard Marie et Pierre Curie, BP 30179, 86962 Futuroscope, France*
[3]*Institut für Aerodynamik und Gasdynamik, Universität Stuttgart, Pfaffenwaldring 21, D-70550 Stuttgart, Germany*

In the present work, laminar flow control, following the discrete roughness elements (DRE) strategy, also called upstream flow deformation (UFD) was applied on a 45° swept-wing at a chord Reynold's number of $Re_c = 2.1 \cdot 10^6$ undergoing cross-flow instability (CFI) induced transition. Dielectric barrier discharge (DBD) plasma actuation was employed at a high frequency ($f_{ac} = 10kHz$) for this purpose. Specialized, patterned actuators that generate spanwise-modulated plasma jets were fabricated using spray-on techniques and positioned near the leading edge. An array of DREs was installed upstream of the plasma forcing to lock the origin and evolution of critical stationary CFI vortices in the boundary layer. Two forcing configurations were investigated - in the first configuration the plasma jets were directly aligned against the incoming CF vortices while in the second the CF vortices passed between adjacent plasma jets. Infrared thermography was used to inspect transition location, while quantitative measurements of the boundary layer were obtained using particle image velocimetry. The obtained results show that the plasma forcing reduces the amplitude of stationary CF modes, thus delaying laminar-to-turbulent transition. In contrast to previous efforts [1], the plasma forcing did not introduce unsteady fluctuations into the boundary layer. The mechanism responsible for the observed transition delay appears to leverage more on localised base-flow modification rather than the DRE/UFD control strategy.

Nomenclature

Symbols

x	Axis normal to the leading edge
y	Axis orthogonal to the chord plane
z	Axis parallel to the leading edge
c	Airfoil chord
α	Angle of attack
uvw	Velocity component along the xyz axes
U	Velocity magnitude
U_∞	Freestream velocity
Re_c	Chord Reynold's number
$\overline{...}$	Time-average
Φ	Power spectral density
λ_z	Spanwise wavelength
w_E	Air-exposed electrode width
w_C	Covered electrode stem width
o	Relative electrode overlap
V_{pp}	Peak-to-peak voltage
f_{ac}	Carrier frequency
T_x	Thrust generated along x
c_μ	Momentum coefficient

Abbreviations

CF	Cross-Flow
CFI	Cross-Flow Instability
UFD	Upstream Flow Deformation
DRE	Discrete Roughness Elements
BFM	Base-Flow Modification
DBD	Dielectric Barrier Discharge
PET	Polyethylene Terephthalate
IR	Infra-Red
PIV	Particle Image Velocimetry

---

*PhD candidate, srikar.yadala.venkata@univ-poitiers.fr

†PhD candidate (currently at Karlsruhe Institute of Technology, Germany), marc.hehner@kit.edu

‡Researcher, j.serpieri@tudelft.nl

§Associate Professor, nicolas.benard@univ-poitiers.fr, AIAA senior member

¶Assistant Professor, m.kotsonis@tudelft.nl

I. Introduction

Aerodynamic drag caused by turbulent flow accounts to 40% of the total drag of an aeroplane [2]. A considerable portion of this is related to the flow around the aircraft lifting surfaces. Considering the recent needs for more efficient and carbon-neutral transport, it becomes essential to elucidate the mechanisms leading to turbulent flow and devise strategies for control. Modern jet aeroplanes feature wings with swept leading edges to postpone the critical Mach number. Around these wings, a full three-dimensional flow develops leading to a secondary flow within the boundary layer, perpendicular to the outer inviscid streamline. This flow component is called cross-flow (CF) and is a result of an imbalance (with respect to the inviscid streamline condition) between the pressure and inertial forces in the boundary layer [3]. The CF component forms an inflection point which leads to the inviscid cross-flow instability (CFI) characterised by co-rotating vortices of stationary (steady) and travelling (unsteady) nature, depending on the relative magnitude of the different types of external disturbances [4, 5]. A detailed review on this topic can be found in [3].

Cross-flow instability plays an important role in laminar-to-turbulent transition in swept-wing boundary layers. Different control strategies have been proposed and investigated to control CFI induced transition (see [1] for a brief review). One such strategy is based on the use of discrete roughness elements (DRE), first proposed by Saric and co-workers [6] and later generalised as upstream flow deformation (UFD) by Kloker and co-workers [7]. Primary stationary CFI appear in a band of unstable wavenumbers. The most unstable (critical) modes amplify and eventually undergo secondary instability leading to transition. The DRE/UFD strategy is based on forcing sub-critical (shorter wavelength) CFI modes, which deter the growth of the critical mode, thus delaying transition. While initial wind-tunnel tests [3, 8] and numerical simulations [7, 9] have successfully delayed transition, later flight tests [10] were inconclusive. In summary, the success of this technique appears to be a strong function of several parameters pertaining to transition evolution (e.g. surface roughness, free stream turbulence, Reynolds number, pressure distribution) [5, 11].

An alternate control strategy named base-flow modification (BFM) is based on the direct suppression of the cause of the instability: the CF component in the boundary layer. Direct numerical simulations employing wall suction [12] or body force [13] have proven to delay transition. [13] achieved BFM by applying a body force against the local CF and observed a reduction in the amplification rates of both the stationary and travelling CFI modes. Thus, the applied forcing stabilizes the boundary layer, by a modification of the mean flow, rendering its performance independent of the nature of CFI and, yielding transition delay. Recently, this strategy was demonstrated experimentally for the first time by applying the necessary body force using a dielectric barrier discharge (DBD) plasma actuator [14] and laminar-to-turbulent transition delay was achieved.

Alternating current DBD actuators work on the principle of air ionisation. Through Coulombian interaction, the actuators transfer momentum to the surrounding air particles, thus resulting in localised acceleration (see [15] for a good description of the basic principles). While DBD actuators have been employed extensively for flow control applications in two-dimensional boundary layers (see [16]), application of these actuators in three-dimensional boundary layers, dominated by CFI is still limited [1, 8, 9, 13, 14, 17, 18]. In the present study DBD actuators are employed to realize DRE/UFD strategy to control CFI induced transition in swept-wing boundary layers. Furthermore, the results obtained are compared to those obtained by [14] employing the BFM strategy.

II. Experimental Set-up

A. Swept wing model, wind tunnel and reference systems

The model used in the current investigation is a 45° swept-wing of 1.25 m span and 1.27 m chord in the free stream direction. The airfoil used is a modified version of the NACA 66018 shape named *66018M3J*. The experiments were carried out in a closed-loop, low-turbulence tunnel (LTT) at TU Delft. The tunnel's testing chamber dimensions are 1.25 m × 1.80 m × 2.6 m in height, width and length, respectively. More details of the swept-wing model and the wind tunnel can be found in [19]. For the entire experiment, the swept-wing was at an incidence angle of $\alpha = 3^\circ$ and the flow over the wing's pressure side was investigated. The freestream velocity was set at $U_\infty = 25\ \mathrm{ms}^{-1}$ corresponding to a chord Reynold's number $Re_c = 2.1 \cdot 10^6$. For this flow configuration, the pressure minimum point is at $x/c = 0.63$.

Stationary CFI modes were forced using an array of DRE, at a spanwise wavelength of $\lambda_{z,crit} = 8$ mm which, for the investigated flow conditions, is the critical stationary CFI mode as predicted by linear stability theory. This is done because for the studied flow conditions, natural transition (i.e. no DREs) is downstream of the pressure minimum and is dominated by laminar separation [1]. DRE forcing assists in bringing transition upstream, achieving CFI-dominated conditions and finally, by conditioning the initial amplitude of the CFI modes, a more spanwise uniform transition front

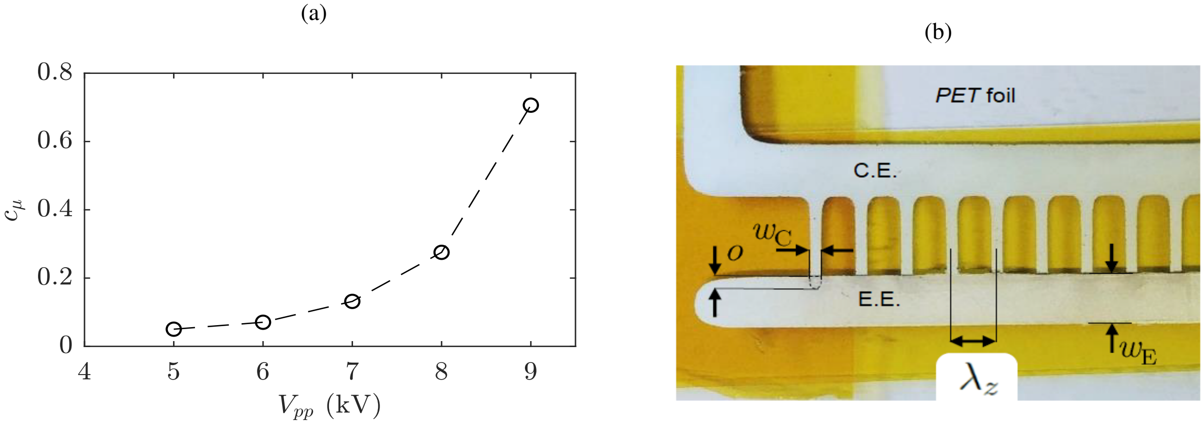

Fig. 1 (a) Variation of momentum coefficient c_μ with input peak-to-peak voltage V_{pp} (f_{ac} = 10 kHz). (b) DBD plasma actuator employed to force monochromatic stationary CFI modes. The dielectric PET foil, the exposed electrode (E.E.), the covered electrode (C.E.), width of the stems (w_C), their wavelength (λ_z), the exposed electrode width (w_E) and the relative overlap between the electrodes (o) are also shown.

is realized. Most importantly, amplification of the critical mode presents a "worst case scenario" for any given control scheme, thus giving a maximum bound on the performance of the control. An array of DREs (with diameter 2 mm and height 60 μm) was installed at $x/c = 0.017$, close to the neutral point of the $\lambda_{z,crit} = 8$ mm to lock this critical CFI mode.

The reference system used in this study is as follows. The swept-wing reference system is represented using xyz. It is such that its x axis is perpendicular to the leading edge of the wing, y axis is perpendicular to the chord plane and z axis is parallel to the leading edge. The corresponding velocity components are represented by uvw. The free-stream velocity is referred to as U_∞.

B. DBD plasma actuators

The investigated boundary layer is highly receptive to surface roughness [3]. Thus it is imperative to maintain minimum protuberance due to the actuator. To ensure this, computer-controlled spraying of micrometric conductive silver particles was employed to fabricate the electrodes of the DBD actuators, with thickness in the order of a few microns. Primary and secondary travelling CFI modes give rise to flow fluctuations in the boundary layer [5, 7, 19]. In numerical studies where DBD actuators are employed to control CFI-induced transition, the actuator is seen to have very little effect on the unsteady modes [9, 13, 20]. This is because, in these studies the actuators are modelled to produce a steady forcing. However, DBD actuators are known to impart unsteady fluctuations [21] which can trigger transition. This was observed in the experimental investigation of [1] who employed DBD actuators to realize the UFD control strategy. Though the actuators successfully conditioned the boundary layer with sub-critical stationary CFI modes, the unsteady forcing of the actuator at $f_{ac} = 2$ kHz lead to the amplification of travelling CFI modes in the frequency band $300 < f < 550$ Hz [19], which resulted in earlier transition. Due to this, they recommended forcing at higher frequencies (also discussed by [20]). Based on these recommendations, forcing at $f_{ac} = 10$ kHz was employed in the current study.

A dedicated experiment using high-speed planar particle image velocimetry (PIV) in quiescent conditions was carried out to characterise the performance of a spanwise-invariant (i.e. straight) DBD actuator with dielectric PET and silver electrodes [14]. The acquired PIV vector fields are used to compute the thrust (T_x) generated at different input AC voltages using the momentum balance method [22]. This thrust is further used to compute the momentum coefficient c_μ by equation 1,

$$c_\mu = \frac{T_x}{\frac{1}{2}\rho u_e^2 \theta_u} \tag{1}$$

where u_e is the local ($x/c = 0.035$) boundary layer edge velocity and θ_u is the local momentum thickness extracted from the boundary layer numerical solution of the corresponding baseline case (no plasma forcing). The variation of c_μ

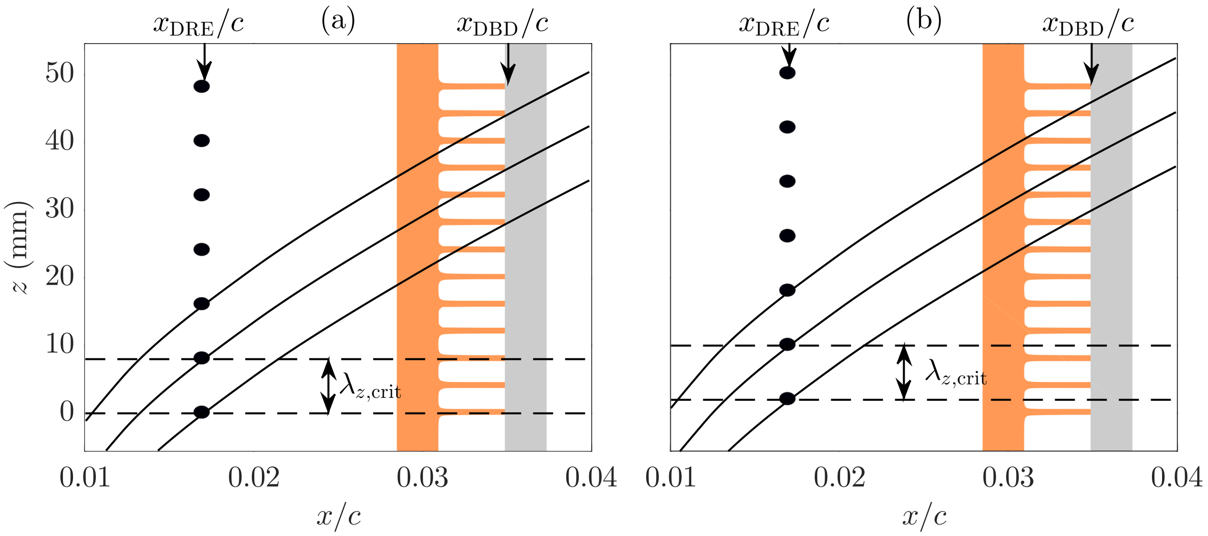

Fig. 2 The investigated forcing configurations. The DRE array (•), the DBD actuator with its encapsulated (orange, with stems) and the air-exposed (gray, straight) electrodes and, three consecutive inviscid streamlines originating at the DRE are shown. (a) UFD4$_{in}$ configuration; (b) UFD4$_{out}$ configuration.

with input voltage for the investigated flow condition is presented in figure 1a. Henceforth, c_μ will be employed to discuss the different forcing conditions.

To realize the UFD strategy, DBD actuators that generate spanwise-modulated plasma jets were designed and fabricated to force a single monochromatic primary CFI mode. The design is shown in figure 1b and is such that the air-exposed electrode is a uniform strip of conductive silver (width $w_E = 5$ mm). The grounded electrode is encapsulated below the dielectric barrier (500 μm thick *polyethylene terephthalate* or PET foil) and is made of a series of equi-spaced stems. The spacing between adjacent stems defines the spanwise wavelength (λ_z) of the plasma forcing and the corresponding stationary CFI mode forced. The stems are 10 mm long and $w_C = 1$ mm wide. They are projected towards the air-exposed electrode with a relative overlap of $o = 2$ mm to ensure consistent plasma formation. The air-exposed electrode was placed downstream to have the induced ionic wind aligned with the $-x$ direction as shown in figure 3b.

The DBD actuator was installed on the swept-wing model such that the electrodes' interface was downstream of the DRE array at $x/c = 0.035$ (see figure 3). The actuator was wrapped around the leading edge to avoid any forward-facing steps and extended to $x/c \approx 0.69$ which is downstream of the pressure minimum point of the airfoil at $x/c = 0.63$ [19]. Additionally, a 50 μm thick layer of *Kapton* polyimide film was placed between the actuator and the model surface to better protect the latter. The air-exposed electrode was supplied with a sinusoidal AC signal of peak-to-peak voltage amplitude between 5 and 8 kV while the encapsulated electrode was grounded. The actuator was powered using a *GBS Electronik Minipuls 4* high-voltage amplifier controlled by *LabView* software suite.

The employed DBD actuator generated spanwise-modulated jets to force sub-critical stationary CF vortices with wavelength $\lambda_z = 4$ mm. By manipulating the relative position of the DBD actuator with respect to the DREs, two different forcing configurations were realized and investigated. Such a study is enabled due to the use of DRE forcing which essentially locked the origin of the forced stationary CFI modes and their eventual growth along the inviscid streamline. For the first forcing configuration, the DBD actuator was installed such that, the incoming inviscid streamline intersects the station $x/c = 0.035$ on the plasma jets as shown in figure 2a. As the stationary CF vortices are roughly aligned with the inviscid streamline, the plasma jets are "in-phase" with the incoming CF vortices (henceforth referred to as UFD4$_{in}$ configuration). For the second configuration, the DBD actuator is displaced along the span (z direction) by 2 mm resulting in the plasma jets being 'out-of-phase' with the incoming CF vortices (henceforth referred to as UFD4$_{out}$ configuration). In this case, the stationary CF vortices pass between two adjacent plasma jets as shown in figure 2b.

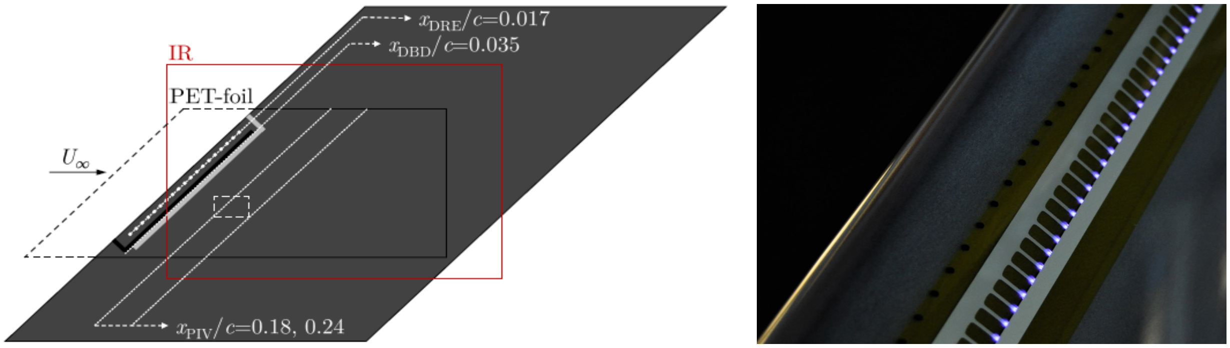

(a) (b)

Fig. 3 (a) Schematic of the performed experiments (not to scale). The flow comes from the left. The electrodes of the DBD actuator (black and grey bars), the outline of the dielectric PET foil (black line, dashed part wrapped around the leading-edge) and the DRE (white dots) are shown. The FOVs of IR thermography (red rectangle) and PIV (dashed white rectangle) are also represented. (b) Image of the swept-wing model's leading edge showing the DREs and the plasma jets generated by the DBD actuator when operated.

C. Infrared thermography

IR thermography was employed to inspect the boundary-layer transition evolution. The convective heat flux from the model surface to the flow is a function of the local wall shear. Regions on the swept-wing model where the flow is turbulent exhibit high shear and thus, cool more rapidly compared to low shear laminar flow regions. This difference in temperature is captured using an IR camera and used for visualisation of the laminar-turbulent transition front [1, 14, 23].

The model was irradiated with six 1kW halogen lamps through the glass windows of the test section to maintain a constant heat flux and enhance contrast. The IR camera used during the experiment was an *Optris PI640*. It features a 640×480 px^2, un-cooled focal plane array that responds to the electromagnetic spectral range between 7.5-13 μm. Its thermal sensitivity (NETD) is 75 mK. The IR camera too was placed outside the wind tunnel, about 1m from the swept-wing model and imaged it through an opportune window. The camera was equipped with a $15^\circ \times 11^\circ$, wide angle lens with a focal depth of 41.5mm. This made it possible to visualise the flow over the entire swept-wing model (see figure 3a). To plot these IR images in the xz plane, a dewarping/deskewing of the images is applied using an opportune calibration image, thus shedding the wing surface curvature. The imaged field of view (FOV) after the dewarping was 1180×725 mm^2. The camera acquired 100 IR fields at a rate of 5Hz for every tested flow case which is averaged to increase the signal-to-noise ratio and presented here. Since quantification of pertinent features such as transition location and CFI wavelength is only dependent on thermal gradients, the results presented here are the raw output of the IR camera and no quantitative temperature data was used.

D. Particle Image Velocimetry

High speed, planar PIV was employed for the quantification of the boundary layer. The inspected plane is along the $x - z$ directions and is about 1mm from the model surface. The planes are centred around $x/c = 0.2$ of the model as shown in figure 3a (dashed white rectangle). Two cameras installed outside the wind tunnel at about 1m from the measured plane were imaging the FOV through opportune optical windows. The cameras used in this study are *Photron FastCAM SA1* featuring a 1024×1024 px^2 sensor, pixel size of 20 μm and 12 bits of digital resolution. The active sensor of each camera was reduced to 512×512 px^2. The cameras were equipped with a *Nikon Nikkor 200mm micro* lens operated at $f_\sharp = 5.6$. The resulting magnification factor of each camera is $M = 0.22$. The two cameras were placed adjacent to each other such that their respective FOVs overlap each other by 5mm. The fields captured by both the cameras were later stitched using a *MatLab* script, resulting in a final FOV of 76×32 mm^2. A Nd:YAG high speed *Continuum Mesa PIV* laser (18 mJ per pulse) was employed for particle illumination from downstream. The laser head was also placed outside the wind tunnel and the light beam was shaped into a 1mm thick light sheet using opportune laser optics. The laser sheet was oriented to be parallel to the model along the entire imaged domain.

The flow was seeded with atomised *Safex* water glycol injected downstream of the testing chamber. The average particle diameter is 1 μm. The laser and the two cameras were synchronized using a *Lavision High Speed Controller* and *Lavision Davis 8.3.1* suite. Image acquisition, pre-processing and correlation were performed using the same

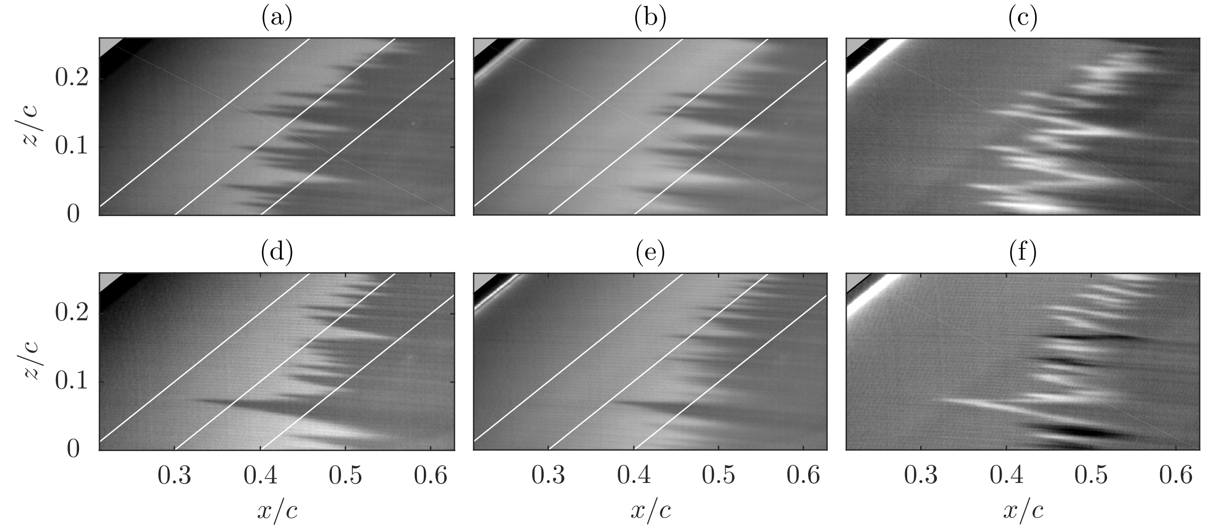

Fig. 4 IR thermography mean fields. The flow comes from the left. The IR mean fields are dewarped and plotted in the xz plane. (a) UFD4$_{in}$ baseline (no plasma forcing); (b) $c_\mu = -0.28$; (c) Subtraction of (a) from (b); (d) UFD4$_{out}$ baseline; (e) $c_\mu = -0.28$; (f) Subtraction of (d) from (e). The solid white lines represent constant chord positions.

software package. Cross-correlation was carried out with a final interrogation window of 24×24 px^2 with a relative overlap of 75%. The final vector spacing is 0.5 mm. The acquisition rate during all the tested cases was 20kHz in single-frame mode. Thus, the pulse separation between subsequent frames was 50 μs. A sequence of 20000 image pairs were acquired using both the cameras for every tested flow case. The resulting measurement time was 1s per test case.

III. IR thermography flow visualisation

The flow topology of the investigated flow conditions, visualized using IR thermogrpahy is presented in figure 4. The flow comes from the left. The upper left-corner of these images is masked as it falls upstream of the swept-wing leading edge. In the baseline (no plasma forcing) cases shown in figures 4a and d, the DBD actuators configured for UFD4$_{in}$ and UFD4$_{out}$ forcing respectively, are installed on the swept-wing but not operated. The flow arrangement observed is the direct result of the DRE array applying a steady forcing at the critical wavelength $\lambda_{z,crit} = 8$ mm. In both cases, the laminar breakdown occurs along the characteristic jagged pattern reported for stationary CFI-induced transition [3, 5, 19, 23]. However, in the baseline case of UFD4$_{out}$ forcing, a large turbulent wedge is noticed which can be the result of some dust particles upstream or some irregularity in one of the attached DREs. Below this wedge, the laminar region spans further downstream compared to the UFD4$_{in}$ forcing baseline case.

The flow topology when the $\lambda_z = 4$ mm CFI mode is forced using the respective DBD actuator at momentum coefficient of $c_\mu = -0.28$ is presented in figures 4b and e. To visualize the movement of the transition front better, figures 4c and f show the subtraction of the IR fields with plasma forcing from their respective baseline case. In both cases, the laminar-to-turbulent transition shifts downstream with plasma forcing, which is evident from the bright area in figures 4c and f.

A distinct streaky pattern in the IR fields is evident in the laminar regions (figure 4). As shown previously by [1], these streaks are the footprints of the primary modes of CFI. Their stationary nature provides the opportunity to quantify their spatial wavelength and its respective evolution in the streamwise direction. The wavenumber power spectral density for the tested cases is shown in figure 5. The dominance of the DRE-triggered $\lambda_{z,crit} = 8$ mm mode is evident in all cases. However the relative decrease in spectral energy of this mode in the cases with plasma forcing is noteworthy. This further reconciles with the observed transition delay. Furthermore, the $\lambda_z = 4$ mm mode forced by the DBD actuators is not observed in both the configurations with $c_\mu = -0.28$ forcing (figures 5c and d). Unfortunately, due to FOV limitations, it is not possible at this stage to asses particularities pertaining to the $\lambda_z = 4$ mm CFI mode close to the forcing location.

Experimentally determined transition-front displacement extracted from the time-averaged IR fields for different

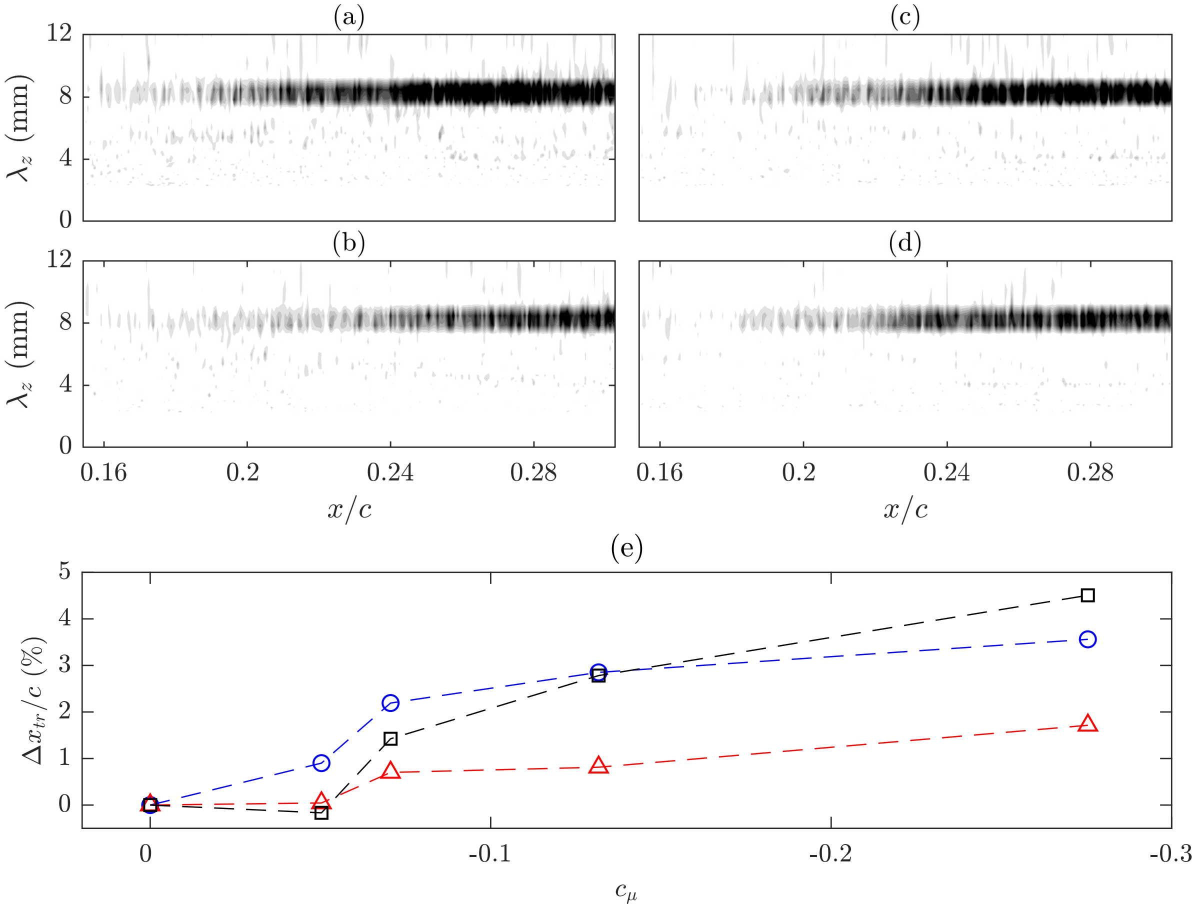

Fig. 5 (a) and (b) wavenumber power spectral density of the IR pixels intensity along the chord of UFD4$_{in}$ baseline and $c_\mu = -0.28$ cases respectively. (c) and (d) wavenumber power spectral density of UFD4$_{out}$ baseline and $c_\mu = -0.28$ cases respectively. (e) Experimentally determined transition-front displacement ($\Delta x_{tr}/c$) versus momentum coefficient c_μ (◯ (blue): UFD4$_{in}$, △ (red): UFD4$_{out}$, □ (black): DBD actuator performing base-flow modification, reproduced from [14]).

plasma forcing conditions are presented in figure 5e. In both UFD4$_{in}$ and UFD4$_{out}$ forcing configurations, the delay in transition due to plasma forcing is proportional to the momentum input c_μ. For the UFD4$_{in}$ configuration, the largest achieved transition delay is about 3.5% of chord, occurring at the highest tested momentum input of $c_\mu = -0.28$. For the UFD4$_{out}$ forcing configuration, the largest achieved transition delay is about 1.7% of chord, thus only half of what was achieved with the UFD4$_{in}$ configuration. Thus, the position of the spanwise-modulated plasma jets relative to the incoming stationary CF vortices seems to have an impact on the success of the control. Studying the acquired PIV mean fields will shed more light on the underlying phenomenon of both these forcing configurations.

A reduction in the transition-front width suggests the amplification of travelling CFI modes [1, 5], as these unsteady modes disturb the stationary CFI modes in the boundary layer, resulting in a more spanwise-uniform transition front. The transition fronts observed in figure 4 show no such reduction in width due to the plasma forcing which suggests that the fluctuations in the frequency band of the travelling CFI modes for the tested flow conditions were not amplified by the unsteady forcing of the DBD plasma actuator.

The transition-front displacements obtained by [14] when the base-flow modification control strategy was applied using DBD plasma actuators at the same flow conditions is also presented in figure 5e (□). The same (in amplitude and wavelength) passive forcing of the critical mode was applied. The transition front is observed to move downstream with c_μ here as well. The largest transition delay achieved in the presented flow cases is about 4.5%. The transition delays achieved by the BFM strategy and the UFD4$_{in}$ forcing configuration at different c_μ are quite similar. The difference is about 0.5% chord on average.

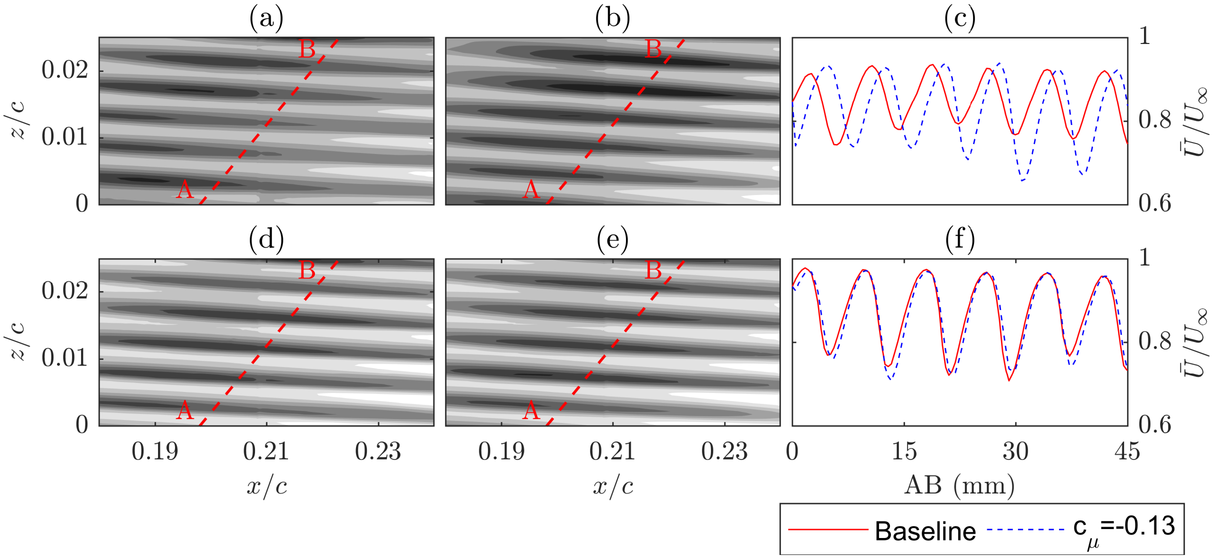

Fig. 6 Time-averaged U velocity fields (9 levels from 0.6 (black) to $1 \cdot U_\infty$ (white)). The flow comes from the left. (a) UFD4$_{in}$ baseline; (b) $c_\mu = -0.13$; (c) Spanwise fluctuation of $\bar{U}$ velocity signal sampled along (dashed red) line AB in fields (a) and (b); (d) UFD4$_{out}$ baseline; (e) $c_\mu = -0.13$; (f) Spanwise fluctuation of $\bar{U}$ velocity signal sampled along (dashed red) line AB in fields (d) and (e).

IV. PIV Velocity fields

Time-averaged velocity magnitude (U) fields of the two forced conditions are presented in figure 6. These fields are non-dimensionalised with the freestream velocity $U_\infty = 25$ ms^{-1}. The baseline cases for UFD4$_{in}$ and UFD4$_{out}$ forcing configurations are shown in figures 6a and d. The role of the DRE forcing in conditioning the laminar boundary layer is clearly visible in these vector fields. The DRE forcing leads to a mean-flow deformation which is seen in the acquired velocity fields as spanwise velocity modulation, with five local minima equally spaced at $\lambda_{z,crit} = 8$ mm. This is also evident in the spanwise mean velocity ($\bar{U}$) signal sampled along (dashed red) line AB in these fields, presented in figures 6c and f (solid red line).

When $c_\mu = -0.13$ forcing is applied on the boundary layer with the UFD4$_{in}$ configuration (figure 6b), the local minima are lower. This results in a stronger spanwise velocity modulation than the corresponding baseline case. A downstream shift of the local minima in the stationary CFI modes is also evident. Moreover, the CF vortices appear to be shifted along the z direction due to the plasma forcing (figure 6c). When $c_\mu = -0.13$ forcing is exerted with the UFD4$_{out}$ configuration (figure 6e), no significant effect is observed on the magnitude of the local minima or the strength of the velocity modulation as seen in figure 6f. This corroborates well with the results of IR flow visualization which showed that forcing with the UFD4$_{out}$ configuration produces lesser delay in transition than the UFD4$_{in}$ configuration.

DBD plasma actuators have been successful in conditioning the swept-wing boundary layer by forcing monochromatic primary CFI modes [1, 8]. Recently, [1] successfully forced sub-critical, critical and super-critical CFI modes using DBD plasma actuators on the same swept-wing model used here. In the current study, although the DBD actuators apply sub-critical forcing at $\lambda_z = 4$ mm on the boundary layer, the spanwise wavelength of the CFI modes is still $\lambda_{z,crit} = 8$ mm (see dashed blue lines in figures 6c and f). It is possible that the DBD actuators force the $\lambda_z = 4$ mm mode which saturates and leads to the onset of the critical mode upstream of the PIV field of view. Another probable cause is the amplification of the critical mode by the DRE array, which renders the momentum imparted by the DBD actuator as insufficient. Thus the actuator fails to force the intended $\lambda_z = 4$ mm sub-critical CFI mode.

The second scenario also explains the difference in the results obtained from the UFD4$_{in}$ and UFD4$_{out}$ configurations. As seen in figure 2b, with the UFD4$_{out}$ configuration, the CF vortices pass between adjacent plasma jets. Thus, the DBD actuator has very little impact on the DRE-triggered stationary CFI modes. With the UFD4$_{in}$ configuration (figure 2a), the CF vortices pass over the plasma jets. Thus the DBD actuator imparts momentum directly against the incoming stationary CF vortices, thus reducing their amplitude and stabilizing the boundary layer and, resulting in a delay of laminar-to-turbulent transition. This mechanism is similar to a localized form of base-flow modification [13, 14]. This is also supported by the comparison of transition delay achieved by the UFD4$_{in}$ forcing configuration and the BFM

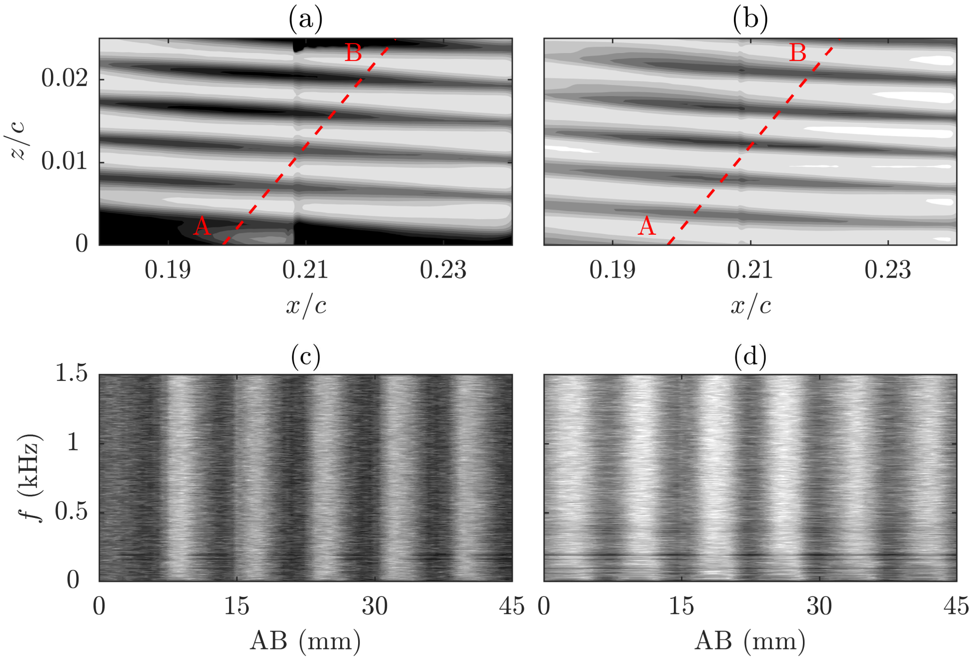

Fig. 7 (a) and (b) standard deviation of the U-velocity fields (10 levels from 0 (white) to $0.13 \cdot U_\infty$ (black)) for the UFD4$_{in}$ forcing configuration. The flow comes from the left. The fields show the baseline and $c_\mu = -0.13$ forcing cases respectively; (c) and (d) non-dimensional normalised power spectra ($\Phi_{U'} \cdot \delta_f / U_\infty^2$, $\delta_f = 2$ Hz) of the U'velocity signal sampled along (dashed red) line AB in (a) and (b) (10 levels from -90 dB (white) to -40 dB (black)).

control strategy shown in figure 5e. As discussed earlier, the achieved transition delay of these two methods is quite comparable. This also suggests that every second plasma jet likely has limited effect on the boundary layer. Further research to visualize and quantify the boundary layer at the forcing location is necessary to confirm these hypotheses.

Statistical analysis and spectral characteristics

The standard deviation of the U-velocity fields of the UFD4$_{in}$ forcing configuration are presented in figures 7a and b. The baseline case shows alternating low and high levels of fluctuations along the span. The flow fluctuations appear to be enhanced only in the regions of the stationary CF vortices due to the introduction of strong velocity shears [24, 25]. In this field, very high levels of fluctuations are observed below $z/c \approx 0.005$, which is attributed to PIV data corruption due to insufficient illumination. When the DBD actuators are operated at $c_\mu = -0.13$, the level of velocity fluctuations is observed to decrease. This suggests that the boundary layer features reduced fluctuations and thus is less prone to undergo breakdown due to unsteady perturbations, in comparison to the baseline.

The U'-velocity signal of the flow fluctuations was sampled along the (dashed red) line AB in figures 7a and b and analysed in the Fourier domain. The power spectral density was computed with a final frequency resolution of $\delta_f = 2$ Hz. The spectra is normalised with Parseval's theorem (see [1], equation 2.1) and non-dimensionalised with U_∞^2. These results are presented in figures 7c and d. Contours in the frequency band $0 < f < 1500$ Hz are plotted, to visualize the effect of plasma forcing on the primary travelling CFI modes which appear at such low frequencies [19]. The baseline flow case shows alternating regions of low and high spectral energy along the span corresponding to the forced stationary CF vortices. The energy is almost equally distributed along the entire frequency range, except at $f \approx 200$ Hz where the energy seems to be enhanced. A region of high spectral energy is observed at the left edge of figure 7c. This is a result of the erroneous fluctuations seen at the bottom of figure 7a.

With the operation of the DBD actuator at $c_\mu = -0.13$ (figure 7d), the travelling CFI frequency band ($300 < f < 550$ Hz) is clearly visible suggesting that the forcing increases the fluctuations in this band. Although, when compared to the baseline case, a decisive reduction in the fluctuations energy within the presented frequency domain is evident. This corroborates well with the results of IR flow visualisation where no reduction in the transition-front width was observed.

As discussed earlier, applying plasma forcing at f_{ac} = 2 kHz lead to the amplification of fluctuations in the travelling CFI frequency band, thus advancing transition [1]. The presented results also confirms the recommendation of [1] regarding the use of high AC frequencies to operate the DBD actuator for swept-wing transition control applications.

V. Concluding remarks

In the present experimental investigation, stationary CF-induced transition in a 45° swept-wing boundary layer is delayed using DBD plasma actuators. An actuator that generates spanwise-modulated plasma jets is fabricated using computer-controlled spraying technique and installed close to the leading-edge such that, it imparts momentum against the incoming flow (along $-x$ direction). The DBD actuator is designed to force sub-critical stationary CFI modes (λ_z = 4 mm) to realize the UFD flow control strategy [3, 7]. The actuator is operated at an AC frequency of f_{ac} = 10 kHz following the recommendation of [1], to avoid the amplification of unsteady fluctuations in the boundary layer due to the unsteady forcing of the DBD actuator.

An array of DREs forcing the critical stationary mode for the investigated flow conditions ($\lambda_{z,crit}$ = 8 mm) is installed just upstream of the DBD plasma actuator to lock the location of the stationary CF vortices and provide a "worst-case scenario" to test the effectiveness of the control (similar to the study by [14]). Two forcing configurations were investigated. In the first, the DBD actuator is positioned such that the stationary CF vortices originating at the DREs pass over the generated plasma jet (UFD4$_{in}$ configuration) thus perceiving the full impact of the plasma body force. While in the second, the stationary CF vortices pass the DBD actuator between two adjacent plasma jets (UFD4$_{out}$ configuration).

Detection and quantification of the transition-front location is performed with IR thermography. A transition delay is achieved with both forcing configurations. However, the delay achieved with the UFD4$_{out}$ configuration is about half of that achieved by the UFD4$_{in}$ configuration. This is peculiar as forcing the same sub-critical CFI mode should result in comparable transition delays. Thus, the relative position of the plasma forcing with the incoming CF vortices is observed to have an effect on the performance of the control technique.

Quantitative measurements of the boundary layer were obtained using high-speed planar PIV. The time-averaged fields show that the boundary layer is conditioned by $\lambda_{z,crit}$ = 8 mm CFI mode forced by the DREs. While, previous studies have shown the ability of DBD actuators to force stationary CFI modes at the forced wavelength [1, 8], no spanwise modulation of velocity at the sub-critical mode forced by the employed actuators is observed. It is not clear whether the boundary layer underwent localised base-flow modification [13, 14] and not upstream flow deformation (UFD). Additionally, studying the unsteady PIV fields show that forcing at f_{ac} = 10 kHz did not amplify unsteady fluctuations in the boundary layer. This is also confirmed by width of the transition fronts measured using IR thermography which shows no difference due to plasma forcing [5].

Further research and analysis is necessary to confirm the mechanism that leads to transition delay in the current study. Flow visualization and quantification close to the forcing location will shed more light on this phenomenon. While transition delay is successfully achieved, application of these actuators to higher Reynold's number flows might render it ineffective due to the increase of the travelling-wave frequency band. Thus, future upscaling of the plasma forcing to higher Reynold's number is necessary.

Acknowledgments

S. Yadala is funded by the French Government programme 'Investissements d'Avenir' (LABEX INTERACTIFS, reference ANR-11-LABX-0017-01). The authors are thankful to Dr M. Kloker and Dr. P. Dörr (Institut für Aerodynamik und Gasdynamik, TU Stuttgart) for their support and many fruitful discussions.

References

[1] Serpieri, J., Yadala Venkata, S., and Kotsonis, M., "Conditioning of cross-flow instability modes using dielectric barrier discharge plasma actuators," *J. Fluid Mech.*, Vol. 833, 2017, pp. 164–205.

[2] Bushnell, D., "Aircraft drag reduction - a review," *Proc. Inst. Mech. Eng., G*, Vol. 217, No. 1, 2003, pp. 1–18.

[3] Saric, W., Reed, H., and White, E., "Stability and transition of three-dimensional boundary layers," *Annu. Rev. Fluid Mech.*, Vol. 35, No. 1, 2003, pp. 413–440.

[4] Bippes, H., “Basic experiments on transition in three-dimensional boundary layers dominated by crossflow instability,” *Progress in Aerospace Sciences*, Vol. 35, No. 4, 1999, pp. 363–412.

[5] Downs, R., and White, E., “Free-stream turbulence and the development of cross-flow disturbances,” *J. Fluid Mech.*, Vol. 735, 2013, pp. 347–380.

[6] Saric, W., Carrillo R.B., J., and Reibert, M., “Leading-edge roughness as a transition control mechanism,” *AIAA* Paper 1998-781, 1998.

[7] Wassermann, P., and Kloker, M., “Mechanisms and passive control of crossflow-vortex-induced transition in a three-dimensional boundary layer,” *J. Fluid Mech.*, Vol. 456, 2002, pp. 49–84.

[8] Schuele, C., Corke, T., and Matlis, E., “Control of stationary cross-flow modes in a Mach 3.5 boundary layer using patterned passive and active roughness,” *J. Fluid Mech.*, Vol. 718, 2013, pp. 5–38.

[9] Dörr, P., and Kloker, M., “Crossflow transition control by upstream flow deformation using plasma actuators,” *J. Appl. Phys.*, Vol. 121, No. 6, 2017, p. 063303.

[10] Saric, W., West, D., Tufts, M., and Reed, H., “Flight Test Experiments on Discrete Roughness Element Technology for Laminar Flow Control,” *AIAA* Paper 2015-0539, 2015.

[11] Lovig, E., Downs, R., and White, E., “Passive laminar flow control at low turbulence levels,” *AIAA Journal*, Vol. 52, No. 5, 2014, pp. 1072–1075.

[12] Messing, R., and Kloker, M., “Investigation of suction for laminar flow control of three-dimensional boundary layers,” *J. Fluid Mech.*, Vol. 658, 2010, pp. 117–147.

[13] Dörr, P., and Kloker, M., “Stabilisation of a three-dimensional boundary layer by base-flow manipulation using plasma actuators,” *J. Phys. D: Appl. Phys.*, Vol. 48, 2015, p. 285205.

[14] Yadala, S., Hehner, M., Serpieri, J., Benard, N., Dörr, P., Kloker, M., and Kotsonis, M., “Experimental control of swept-wing transition through base-flow modification by plasma actuators,” *J. Fluid Mech.*, Vol. 844, 2018.

[15] Benard, N., and Moreau, E., “Electrical and mechanical characteristics of surface AC dielectric barrier discharge plasma actuators applied to airflow control,” *Exp. Fluids*, Vol. 55, No. 11, 2014, pp. 1–43.

[16] Grundmann, S., and Tropea, C., “Active cancellation of artificially introduced Tollmien–Schlichting waves using plasma actuators,” *Exp. Fluids*, Vol. 44, No. 5, 2008, pp. 795–806.

[17] Shahriari, N., Kollert, M., and Hanifi, A., “Control of a swept-wing boundary layer using ring-type plasma actuators,” *J. Fluid Mech.*, Vol. 844, 2018, pp. 36–60.

[18] Yates, H., Juliano, T., Matlis, E., and Tufts, M., “Plasma-Actuated Flow Control of Hypersonic Crossflow-Induced Boundary-Layer Transition in a Mach-6 Quiet Tunnel,” *AIAA* Paper 2018-1076, 2018.

[19] Serpieri, J., and Kotsonis, M., “Three-dimensional organisation of primary and secondary crossflow instability,” *J. Fluid Mech.*, Vol. 799, 2016, pp. 200–245.

[20] Dörr, P., and Kloker, M., “Transition control in a three-dimensional boundary layer by direct attenuation of nonlinear crossflow vortices using plasma actuators,” *Int. J. Heat and Fluid Flow*, 2016, pp. 449–465.

[21] Benard, N., Noté, P., and Moreau, E., “Highly time-resolved investigation of the electric wind caused by surface DBD at various ac frequencies,” *J. Electrostatics*, Vol. 88, 2017, pp. 41–48.

[22] Kotsonis, M., Ghaemi, S., Veldhuis, L., and Scarano, F., “Measurement of the body force field of plasma actuators,” *J. Phys. D: Appl. Phys.*, Vol. 44, No. 4, 2011, p. 045204.

[23] Saric, W., Carpenter, A., and Reed, H., “Passive control of transition in three-dimensional boundary layers, with emphasis on discrete roughness elements,” *Phil. Trans. R. Soc. A*, Vol. 369, No. 1940, 2011, pp. 1352–1364.

[24] White, E., and Saric, W., “Secondary instability of crossflow vortices,” *J. Fluid Mech.*, Vol. 525, 2005, pp. 275–308.

[25] Bonfigli, G., and Kloker, M., “Secondary instability of crossflow vortices: validation of the stability theory by direct numerical simulation,” *J. Fluid Mech.*, Vol. 583, 2007, pp. 229–272.